



Prediction of fatigue crack initial stage based on a multiscale damage criterion

Chuntao Luo*, Aditi Chattopadhyay

Department of Mechanical and Aerospace Engineering, Arizona State University, Tempe, AZ 85287, United States

ARTICLE INFO

Article history:

Received 23 December 2009
Received in revised form 30 August 2010
Accepted 17 September 2010
Available online 22 September 2010

Keywords:

Fatigue
Multiscale model
Damage criterion

ABSTRACT

In this paper a multiscale damage criterion for fatigue crack initial stage prediction is introduced. A damage evolution rule based on strain energy density is modified to incorporate crystal plasticity at the microscale (local). A damage tensor that indicates the local damage state is derived using optimization theory. Damage information is passed from local to grain level, bridging microscale and mesoscale in the form of a damage vector via averaging techniques. Finally, the damage evolution rule for a meso representative volume element (RVE), which contains several grains, is calculated through the Kreisselmeier–Steinhauser (KS) function, which can produce an envelope function for multiobjective optimization. The weighted averaging method is also used to obtain the corresponding damage evolution direction for the meso RVE. A critical damage value is derived in this paper to complete the damage criterion for fatigue life prediction. Simulation results and comparison with experimental data are presented.

© 2010 Elsevier Ltd. All rights reserved.

1. Introduction

Damage detection and condition monitoring for current aerospace vehicles requires significant labor and costs. Research in this area has primarily been based on empirical models, Nondestructive Evaluation (NDE) techniques and observations, rather than on fundamental understanding of failure and detection mechanisms [1,2]. In recent years, structural health monitoring (SHM) technologies [3] have emerged as a new tool to specifically address these challenges. The objective of SHM is to develop a framework for damage identification and state awareness of aerospace, civil, and mechanical engineering infrastructures, which can ultimately enhance their reliability and sustainability.

As a fundamental component of SHM, modeling can provide material behavior for sensing and detection as well as provide data for learning algorithms. Cyclic loading is an important common loading condition for aerospace vehicles [4]. From a physics point of view, the associated phenomenon of fatigue inherently involves multiple length scales due to the presence of microcracks (initiation and growth at microscale) or inclusions that are small compared to the large size of structural components (macroscale). Hence, it is necessary to develop a scale dependent physics-based model for accurate simulation to understand material performance/degradation in various operational environments and ultimately to assess the survivability of current aerospace vehicles [5]. A critical challenge in damage detection is the fact that damage at the microscale cannot be detected by off-the-shelf sensors.

Therefore, it is necessary to fuse data from real sensors and modeling for diagnosis and prognosis. A physics-based model must incorporate multiscale damage criteria in order to accurately track crack nucleation and growth. During more than 170 years of study, better fatigue damage models have been achieved with improved understanding of metal fatigue mechanisms [6–9]. Different stages of fatigue have been suggested by researchers according to their understanding of fatigue life. From experimental observations, fatigue cracks usually start at the surface of a structural component. It starts from shear cracks on crystallographic slip planes and gradually grows approximately perpendicular to the external applied load. This two-stage fatigue life was first concluded by Forsyth [10]. To investigate fatigue life in more detail, Schijve [11] divided fatigue into four periods including crack nucleation, microcrack growth, macrocrack growth and failure. Shang et al. [12] suggested similar divisions which includes five stages: early cyclic formation and damage, microcrack nucleation, short crack propagation, macrocrack propagation and final fracture. Based on different mechanisms for different length of cracks, Miller [13,14] introduced three types of cracks: microstructurally small cracks, physically small cracks and long cracks. After that, Ritchie and Lankford [15] proposed a slight change in classification of small cracks from Miller's definition and also provided the corresponding length scales for the different cracks: microstructurally small cracks of critical microstructural dimensions (grain size), physically small cracks (less than 1 mm), mechanically small cracks (several mm) and chemically small cracks (10 mm). In this paper, the first stage of fatigue life, which is dominated by shear crystallographic slip planes, is investigated by numerical simulation. Relevant lengths are chosen considering the crack categories

* Corresponding author.

E-mail addresses: ctluo@asu.edu (C. Luo), aditi@asu.edu (A. Chattopadhyay).

Nomenclature

F	deformation gradient	$dD^{(\alpha)}$	damage parameter increment on slip system α
F^P	plastic component of the deformation gradient	σ_{mr}	memory stress
F^e	elastic component of the deformation gradient	σ_0	endurance limit
L	velocity gradient	σ_f	true fracture stress
L^e	elastic component of the velocity gradient	$\langle \cdot \rangle$	MacCauley bracket
L^P	plastic component of the velocity gradient	$dY^{(\alpha)}$	plastic strain energy increment on slip system α
α	the α^{th} slip system	$\sigma_n^{(\alpha)}$	normal stress on slip system σ
β	the β^{th} slip system	$d\varepsilon^P$	plastic strain increment corresponding to $\sigma_n^{(\alpha)}$
$\dot{\gamma}^{(\alpha)}$	resolved slip rate	$\sigma_s^{(\alpha)}$	shear stress on slip system α
$s^{(\alpha)}$	slip direction	$d\gamma^P$	plastic strain increment corresponding to $\sigma_s^{(\alpha)}$
$m^{(\alpha)}$	normal to the slip plane	$d\bar{D}$	damage tensor increment at microscale
$\tau^{(\alpha)}$	resolved shear stress	\bar{D}	damage vector for each grain
σ	Cauchy stress tensor	θ	weight
$\dot{\gamma}_0^{(\alpha)}$	reference strain rate on slip system α	D_{meso}	damage parameter for meso RVE
n	strain rate exponent	D_c	critical damage value
$g^{(\alpha)}$	current strength of slip system α	l	average grain size
$\chi^{(\alpha)}$	backstress	LHS	critical damage value
h_0	initial hardening modulus	RHS	average grain size
τ_s	stage I stress	ω	surface energy density
τ_0	initial yield stress	A	meso RVE size

defined by Ritchie, e.g. the characteristic crack length for critical damage value is taken as average grain size and meso RVE used is a $1 \text{ mm} \times 1 \text{ mm}$ square which is close to physically small crack size. The methodology for fatigue damage estimation consists of two major parts. First part is to calculate the stress–strain distribution based on a multiscale model. Second part is to apply a developed multiscale fatigue damage criterion based on the stress–strain distribution obtained from the first step to estimate the failure of a meso RVE as well as the potential crack directions in the RVE. It should be aware that most existing damage criteria are applied at the macroscale and in these approaches crack growth and propagation direction are addressed separately using different criteria. In this paper, the developed multiscale fatigue damage criterion can predict crack growth and propagation direction simultaneously.

2. Constitutive model

For crystalline materials it is important to incorporate microstructure, crystallinity and micromechanics into the continuum description of finite strain plasticity. The work of Taylor [16,17] shows that crystal dislocation provides a clear atomistic interpretation of the slip process and strain hardening. They were also able to show how micromechanics could be incorporated into macroscopic analysis of plastic flow. The pioneering work of Taylor was continued by many other researchers including Hill, Rice, Asaro and Bassani [18–24]. Their work illustrated that crystal plasticity is indeed necessary to incorporate important micromechanical features of plastic flow into macroscopic analysis. Single crystal plasticity theory offers several advantages over other techniques and is used in this research to describe the material behavior in the hot-spot of an aluminum structure.

A brief introduction of single crystal plasticity is presented in this section for convenience of the reader. Using the standard multiplicative decomposition assumption, the deformation gradient $F = \partial x / \partial X$ can be decomposed into elastic and plastic components as shown in Fig. 1.

$$F = F^e \cdot F^P \quad (1)$$

Fig. 1 shows that the lattice orientation and spacing remain the same for the plastic deformation of the material while the elastic

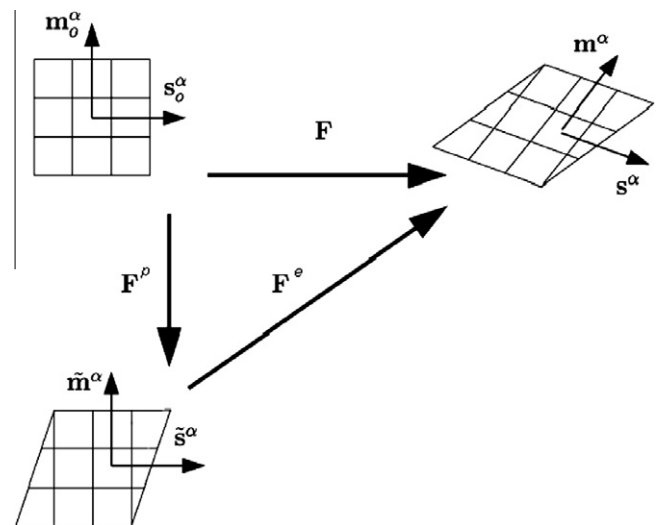


Fig. 1. Multiplicative decomposition of the deformation gradient.

component of the deformation gradient shows stretching and rotation of the lattice compared to the reference configuration. The velocity gradient, $L = \frac{\partial v}{\partial x}$, in the current configuration is related to the deformation gradient by:

$$L = \dot{F}F^{-1} = L^e + L^P \quad (2)$$

where $L^e = \dot{F}^e F^{e-1}$ and $L^P = F^e \dot{F}^P F^{P-1} F^{e-1}$. Assuming that the inelastic deformation of a single crystal arises only from crystalline slip, the plastic velocity gradient can be rewritten in terms of the resolved slip rate, the slip direction and the normal to the slip plane as shown below:

$$L^P = \sum_{\alpha} \dot{\gamma}^{(\alpha)} s^{(\alpha)} \otimes m^{(\alpha)} \quad (3)$$

The resolved shear stress, which plays a vital role in promoting slip, has been derived from the Cauchy stress tensor, by the standard relationship:

$$\tau^{(\alpha)} = \sigma : (s^{(\alpha)} \otimes m^{(\alpha)})_{\text{sym}} \quad (4)$$

It should be clarified that the slip direction and the vector normal to the slip plane used above are defined after deformation, that is, in the “current” configuration. The relationship between the slip systems in the deformed configuration and the ones in the reference configuration can be expressed as follows:

$$s^{(\alpha)} = F^e s_0^{(\alpha)} \text{ and } m^{(\alpha)} = m_0^{(\alpha)} F^{e-1} \quad (5)$$

A power-law is used in the flow rule to calculate the slip increments as follows [25,26]:

$$\dot{\gamma}^{(\alpha)} = \dot{\gamma}_0^{(\alpha)} \left| \frac{\tau^{(\alpha)} - \chi^{(\alpha)}}{g^{(\alpha)}} \right|^n \text{sign}(\tau^{(\alpha)} - \chi^{(\alpha)}) \quad (6)$$

where $g^{(\alpha)}$ and $\chi^{(\alpha)}$ represent the isotropic and kinematic hardening, respectively. The hardening law for $g^{(\alpha)}$ and $\chi^{(\alpha)}$ is presented below:

$$\dot{g}^{(\alpha)} = \sum_{\beta} h_{\alpha\beta} \dot{\gamma}^{\beta} \quad (7)$$

$$\dot{\chi}^{(\alpha)} = b \dot{\gamma}^{(\alpha)} - r \chi^{(\alpha)} |\dot{\gamma}^{(\alpha)}| \quad (8)$$

where $\begin{cases} h(\gamma) = h_0 \text{sech}^2 \left| \frac{h_0 \gamma}{\tau_s - \tau_0} \right|, & \alpha = \beta \\ qh(\gamma), & \alpha \neq \beta \end{cases}$ are called self and latent hardening moduli, respectively. b , r and q are material constants. The cumulative shear strain on all slip systems can be obtained by:

$$\gamma = \sum_{\alpha} \int_0^t |\dot{\gamma}^{(\alpha)}| dt \quad (9)$$

For the numerical simulation, a widely used commercial finite element software ABAQUS [27] is used and a user-defined material subroutine (UMAT) that implements single crystal plasticity is developed based on Huang's work [28]. All the slip systems are treated as potentially active. Since negative $\dot{\gamma}^{(\alpha)}$ is allowed, slip system $(s^{(\alpha)}, m^{(\alpha)})$ and slip system $(-s^{(\alpha)}, m^{(\alpha)})$ are considered as one slip system. The same rule is applied when calculating the damage parameters within each slip system. The results showed in our previous publications [29,30] indicate that the modified UMAT code can capture fatigue hardening and saturation. The most important feature of the model is that single crystal plasticity has the capability to capture local material anisotropic behavior due to different grain orientations.

3. Multiscale damage criterion

3.1. Damage criterion incorporating single crystal plasticity

The work of Jiang et al. [31–33] shows that the fatigue damage criterion they developed has the capability for multiaxial and non-proportional loading. In this model, accumulated fatigue damage is calculated along all directions in three dimensional (3D) space. The critical material plane is determined by checking the plane in which the maximum accumulated fatigue damage reaches a critical value and the direction of crack propagation is along the critical material plane. However, this method is computationally expensive and time inefficient to implement in 3D. Luo et al. extended this energy based damage evolution rule based on the fact that fatigue cracks in metals tend to nucleate and propagate initially along slip planes [29]. In this work, single crystal plasticity is incorporated to the damage evolution rule so that instead of calculating accumulated fatigue damage along all directions in 3D space, calculation was carried out only among potential active slip systems. The corresponding criteria are rewritten as:

$$dD^{(\alpha)} = \left\langle \frac{\sigma_{mr}}{\sigma_0} - 1 \right\rangle^m \left(1 + \frac{\sigma_n^{(\alpha)}}{\sigma_f} \right) dY^{(\alpha)} \quad (10)$$

$$dY^{(\alpha)} = \delta \sigma_n^{(\alpha)} (d\epsilon^p)^{(\alpha)} + \frac{1 - \delta}{2} \sigma_s^{(\alpha)} (d\gamma^p)^{(\alpha)} \quad (11)$$

where m and δ are material constants. It should be noted that the direction of the maximum material plane is a unit vector along the critical plane rather than a normal vector to the plane. This will be further clarified in the results section. In this paper, all the simulations are focused on face centered cubic (FCC) crystal structures, like copper and aluminum. A single FCC crystal has 12 slip systems, comprised of four slip planes, each with three slip directions. The damage parameter evolution of a single grain of aluminum inside the meso RVE for 12 potential active slip systems under uniaxial cyclic loading was presented in our previous work [29]. The grain was oriented for single slip and the results showed that the critical slip plane is approximately 45° to the loading direction.

3.2. Microscale damage tensor

Using Eqs. (10) and (11), the damage parameter $D^{(\alpha)}$ of each slip system can be calculated. In order to incorporate damage information from the 12 slip systems, a damage tensor is developed to indicate the damage status at a particular point. In Eq. (10), the damage parameters in all 12 slip systems are in a strain energy density form. This makes it reasonable to assume that the damage tensor, which is also associated with strain energy density, is a symmetric tensor. On the other hand, it should reflect the directional effects for different slip systems. Thus, the relation between the damage tensor increment and the damage parameter increment in each slip system is developed as follows:

$$dD^{(\alpha)} = m^{(\alpha)} dDs^{(\alpha)}, \alpha = 1, 2, \dots, 12 \quad (12)$$

A symmetric tensor has six independent components, but the resulting 12 conditions obtained from Eq. (12) over constrain the problem and a unique tensor that satisfies all of them simultaneously could not be found. Therefore, an averaged damage tensor is computed using an optimization technique. The objective function in incremental form is shown below:

$$E^2 = \sum_{\alpha=1}^{12} \left[dD^{(\alpha)} - m^{(\alpha)} dDs^{(\alpha)} \right]^2 \quad (13)$$

To minimize the objective function, the necessary condition of optimality (in index notation) is:

$$\frac{\partial E^2}{\partial D_{ij}} = 2 \sum_{\alpha=1}^{12} \left[m_m^{(\alpha)} dD_{m1} s_1^{(\alpha)} m_i^{(\alpha)} s_j^{(\alpha)} - dD^{(\alpha)} m_i^{(\alpha)} s_j^{(\alpha)} \right] = 0 \quad (14)$$

with the constraint $m_i s_i = 0$. The linear equations reduce to a set of five equations. A sixth equation need to be found in order to determine the six components of the damage tensor. As previously mentioned, Eq. (12) is over constrained for all slip systems, thus a constraint is imposed where the sum of the RHS in Eq. (12) equals to the sum of the LHS for all the potential slip systems. The additional equation is as follows:

$$\begin{aligned} & \left[\sum_{\alpha=1}^{12} m_1^{(\alpha)} s_1^{(\alpha)} \right] dD_{11} + \left[\sum_{\alpha=1}^{12} (m_1^{(\alpha)} s_2^{(\alpha)} + m_2^{(\alpha)} s_1^{(\alpha)}) \right] dD_{12} \\ & + \left[\sum_{\alpha=1}^{12} (m_1^{(\alpha)} s_3^{(\alpha)} + m_3^{(\alpha)} s_1^{(\alpha)}) \right] dD_{13} + \left[\sum_{\alpha=1}^{12} (m_2^{(\alpha)} s_2^{(\alpha)}) \right] dD_{22} \\ & + \left[\sum_{\alpha=1}^{12} (m_2^{(\alpha)} s_3^{(\alpha)} + m_3^{(\alpha)} s_2^{(\alpha)}) \right] dD_{23} + \left[\sum_{\alpha=1}^{12} m_3^{(\alpha)} s_3^{(\alpha)} \right] dD_{33} = \sum_{\alpha=1}^{12} dD^{(\alpha)} \end{aligned} \quad (15)$$

The developed procedure is expected to yield a damage tensor capable of predicting damage growth rate and direction of damage evolution simultaneously by computing the maximum eigenvalue

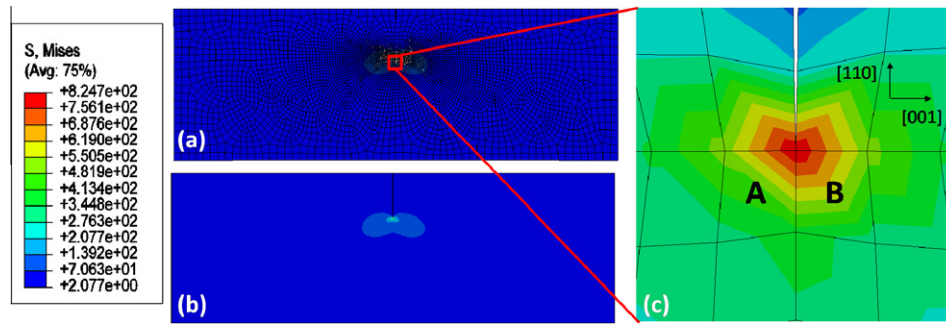


Fig. 2. Simulation for simple tension on a pre-cracked single crystal plate. (a) Mesh of the plate; (b) Mises stress distribution in the plate; (c) Enlarged area at the crack tip.

Table 1
Material properties used for Al2024.

Elastic moduli (GPa)	$D_{1111} = 112, D_{1122} = 59.5, D_{2222} = 114, D_{1133} = 59, D_{2233} = 57.5, D_{3333} = 114, D_{1112} = 1.67, D_{2212} = -0.574, D_{3312} = -1.09, D_{1212} = 26.7, D_{1113} = 1.25, D_{2213} = -0.125, D_{3313} = -1.12, D_{1213} = -1.92, D_{1313} = 26.2, D_{1123} = -1.92, D_{2223} = 1.86, D_{3323} = 0.068, D_{1223} = -0.125, D_{1323} = -1.09, D_{2323} = 24.7$			
Material constants in power law	$n = 10$	$\dot{\gamma}_0 = 0.001 \text{ s}^{-1}$		
Material constants in self and latent hardening	$h_0 = 8.9 \tau_0$	$\tau_s = 1.8 \tau_0$	$\tau_0 = 76 \text{ MP}\alpha$	$q = 1.0$

and the corresponding eigenvector. A simulation for a simple test case is illustrated in Fig. 2. All the material properties for Al2024 used in the model which can be found in authors' previous work [29] are represented in Table 1. The results were slightly counter-intuitive. At some points, the maximum eigenvalue becomes negative, which has no physical meaning. Consequently, the damage tensor is decomposed into deviatoric part and hydrostatic part. Since damage is driven by plasticity and the damage tensor is developed to reflect the slip effect, the deviatoric part of the damage tensor should also contain the necessary information. The maximum eigenvalue and the corresponding eigenvector of the deviatoric part appear to provide reasonable results in the context of damage accumulation.

The corresponding eigenvectors shown in Table 2 for element A which is in front of the crack tip are very close to the experimental results.

Table 2 shows that the damage accumulates almost in the X-Y plane for most of the time and slowly changes its direction from approximately [1 0 0] to [0.756 -5.38 0.00831]. This direction almost lies in the X-Y plane and in the slip plane whose normal is [0.577 0.816 0] as shown in Table 3. It should be noted that all the directions presented in Table 3 are based on global Cartesian coordinates system. By checking element B which lies at the right side of the crack tip, the direction of the corresponding eigenvector and the one on the LHS are symmetric with respect to the [1 1 0] direction. This is in accordance with experimental results observed in Refs. [34,35], with the two potential slip planes being [0.577 0.816 0] and [0.577 -0.816 0].

3.3. Mesoscale damage vector

3.3.1. Kreisselmeier–Steinhauser (KS) function

Damage is believed driven by plastic deformation. Thus, in this paper, the coupling between damage and elasticity was not considered. Besides, the idea of this paper is to bring up a multiscale concept and build up a quantity for a RVE based on current stress-strain distribution which can represent the damage status of the RVE considering some of the microstructure features. Therefore, several optimization methods and averaging techniques are used in this paper to pack the local damage information and transfer it into a global damage variable. For this purpose, a Kreisselmeier–

Table 2
Eigenvector corresponding to the maximum eigenvalue of deviatoric part.

Time(s)	X	Y	Z
7.95E-02	9.20E-01	-1.47E-01	2.22E-01
9.95E-02	8.68E-01	-1.73E-01	3.69E-01
1.10E-01	8.71E-01	-1.88E-01	3.58E-01
1.30E-01	8.27E-01	-3.70E-01	3.63E-01
1.40E-01	8.27E-01	-3.96E-01	3.24E-01
1.90E-01	8.27E-01	-5.02E-01	2.25E-01
2.00E-01	8.23E-01	-5.12E-01	2.27E-01
2.20E-01	8.07E-01	-5.15E-01	2.55E-01
2.30E-01	7.94E-01	-5.10E-01	2.75E-01
2.60E-01	7.59E-01	-4.90E-01	3.27E-01
2.70E-01	7.49E-01	-5.37E-01	-6.77E-03
2.80E-01	7.56E-01	-5.38E-01	8.31E-03

Table 3
Twelve slip systems.

Normal to slip plane	Slip directions
0.577, 0, 0.816	0.707, 0.5, -0.5
	-0.707, 0.5, 0.5
	0, -1, 0
0.577, -0.816, 0	0.707, 0.5, 0.5
	0, 0, 1
	0.707, 0.5, -0.5
0.577, 0.816, 0	0.707, -0.5, 0.5
	0, 0, 1
	-0.707, 0.5, 0.5
-0.577, 0, 0.816	0.707, -0.5, 0.5
	0.707, 0.5, 0.5
	0, -1, 0

Steinhauser (KS) function based approach is used to account for the contribution from all grains to the total damage accumulation at mesoscale. This makes current multiscale model a statistical model rather than a progressive damage model. The KS function based approach incorporates criteria that allow contribution from the more critical grains to be reflected in the damage calculation. Traditionally, KS function is used in optimization applications involving multiple objective functions and/or constraints [36]. From a mathematical point of view, the KS function represents

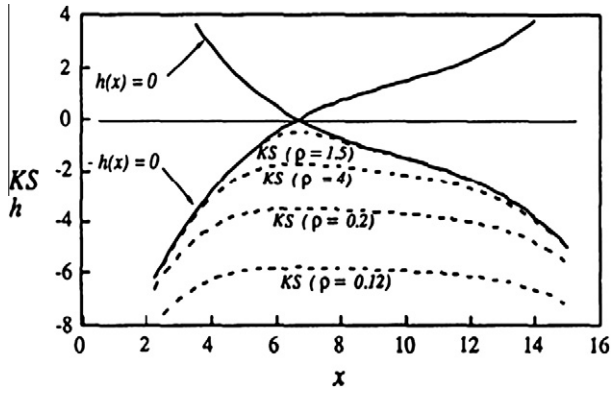


Fig. 3. KS function [36].

an envelope function (for a set of functions), as shown in Fig. 3 and is defined as:

$$KS[g_i(x)] = -\frac{1}{\rho} \ln \left[\sum_i e^{-\rho h_i(x)} \right] \quad (16)$$

where ρ is a parameter which determines the closeness of the KS function to the boundary of the multiple objective functions $h_i(x)$. In current work, the multiple objective functions are the damage growths of all the grains in a meso RVE as functions of the time. When ρ is positive, the KS function is close to the lower bound of $h_i(x)$, and when ρ is negative, the KS function is close to the upper bound of $h_i(x)$. However, Eq. (16) cannot be used directly for calculation because of the exponential term. The simplified KS function form for calculation purposes is derived as:

$$KS[h_i(x)] = \begin{cases} \text{Max}(h_i(x)) + \frac{1}{\rho} \ln \left[\sum_i e^{\rho(h_i(x) - \text{Max}(h_i(x)))} \right], & \text{upper bound} \\ \text{Min}(h_i(x)) - \frac{1}{\rho} \ln \left[\sum_i e^{-\rho(h_i(x) - \text{Min}(h_i(x)))} \right], & \text{lower bound} \end{cases} \quad (17)$$

3.4. Damage parameter and direction at the mesoscale

As mentioned in the introduction, a 1 mm × 1 mm square is chosen as a meso RVE (Fig. 4) according to the length definition of physically small crack by Ritchie. The procedures to create meso RVE mesh comprise two steps. First, an Electron Backscattering Diffraction (EBSD) scan is used to get the microstructure of the material including grain orientations, grain shapes and sizes. Second, a software package OOF (Object-Oriented Finite element analysis from NIST) is used to graphically assign the material properties to a microstructure image and mesh it. It should be pointed out that all the meso RVEs are generated directly from the EBSD scans of the material so that all the grain information used in the FE simulation is kept the same as real microstructure. The grain sizes and shapes can affect the stress–strain distribution in the RVE; consequently can affect the damage prediction to some extent. However, grain size and shape effects are not explicitly considered in the constitutive model. Meanwhile, traditional single crystal plasticity is used to describe the material behavior at the hotspot area of the structural components. Stress/strain gradient effect, which can take account of the size effect in the constitutive model such as the mechanism based strain gradient crystal plasticity (MSG-CP) or other strain gradient theory, is not considered in current work. In order to get the damage parameter and direction at the meso-scale, each grain in the meso RVE (Fig. 4) is treated as a single unit. The output of each grain is a damage vector \vec{D} obtained by using an averaging technique. Three simple steps are carried out to calculate

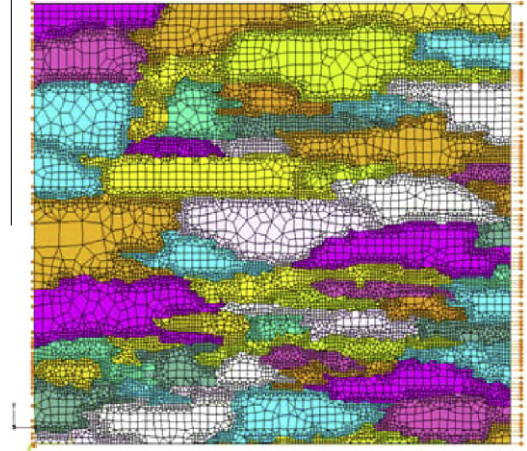


Fig. 4. Meso RVE containing different oriented grains.

this damage vector of each grain. First, the deviatoric part of the damage tensor is calculated for each element within a grain. Next, the deviatoric damage tensors of all the elements in the grain are averaged to get one averaged damage tensor in which each component of this damage tensor comes from the mean value of the corresponding components of all the elements' deviatoric damage tensor. Finally, the damage vector of each grain is calculated where the magnitude of the damage vector, D , is set equal to the maximum eigenvalue of the averaged damage tensor. The damage vector lies along the corresponding eigenvector.

The magnitude of the damage vector, D , in each grain is a function of time. The upper and lower bound for D of all the grains within a meso RVE can be obtained by applying the KS function. Then the damage index for the meso RVE can be defined as:

$$D_{meso} = (\theta KS_u + (1 - \theta)KS_l) / D_c \quad (18)$$

where θ is related to the critical damage value which is defined in Eq. (19), total grain damage and the total number of grains within a meso RVE. It measures the number of grains that reaches the critical damage value, D_c . The critical damage value is also used to determine crack initiation in the meso RVE. The damage direction in the meso RVE can be obtained by normalizing the sum of all damage vectors for all grains. For prediction of fatigue crack initiation, the criteria should be related to the local damage parameter, i.e. the damage parameter D of each grain. When the maximum damage parameter of each grain within a meso RVE reaches the critical damage threshold, the corresponding number of fatigue cycles is treated as fatigue crack initiation and the corresponding grain with the maximum damage parameter is regarded as the crack initiation spot. The goal of using a damage index for meso RVE, D_{meso} , is to determine the failure of the RVE by checking whether D_{meso} reaches 1 or not. In this paper, for convenience of experimental validation, the failure crack length of the meso RVE is taken as 1 mm considering the size of the meso RVE and the resolution of the digital image acquisition system used in the experiments. The meso RVE size is about 1 mm × 1 mm and only the failure of the meso RVE is validated considering our current experimental capabilities.

3.5. Critical damage value for crack nucleation

For aluminum, the surface energy density [37] ω , which corresponds to the energy variation per unit area due to the creation of surface at room temperature, is 865.18 MJ/m². In order to initiate a crack, the minimum energy required should be $2 \times 865.18 \times l \times t$, where 2 indicates there are two free surfaces for a crack. Parameters l and t are the characteristic length and width of the crack

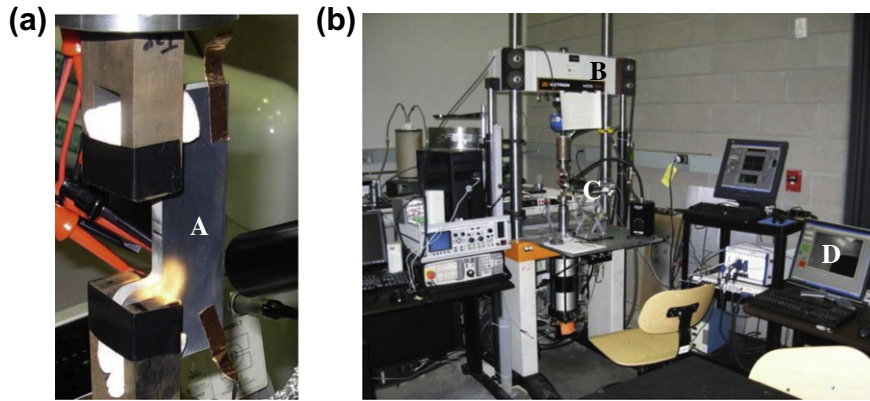


Fig. 5. Lab setup for fatigue tests of structural components with digital image acquisition system monitoring the crack length: (A) lug joint sample; (B) hydraulic frame; (C) CCD camera; (D) digital image acquisition system.

Table 4
No. of cycles to get 1 mm crack for different lug joint samples in fatigue tests.

Lug joint specimens	No. of cycles to obtain 1 mm crack
Sample 1	213 k
Sample 2	220 k
Sample 3	223 k
Sample 4	125 k

surface, respectively. In the simulation, l is chosen to be the average grain size obtained from an EBSD scan. In order to determine the critical damage value, an assumption is made that the cumulative damage due to plastic deformation in the meso RVE should be greater than the minimum energy for creating two free surfaces of a crack. The width of the meso RVE is chosen to be the same as the crack width so that the critical damage value is only a function of the average grain size l , the meso RVE size A and the surface energy

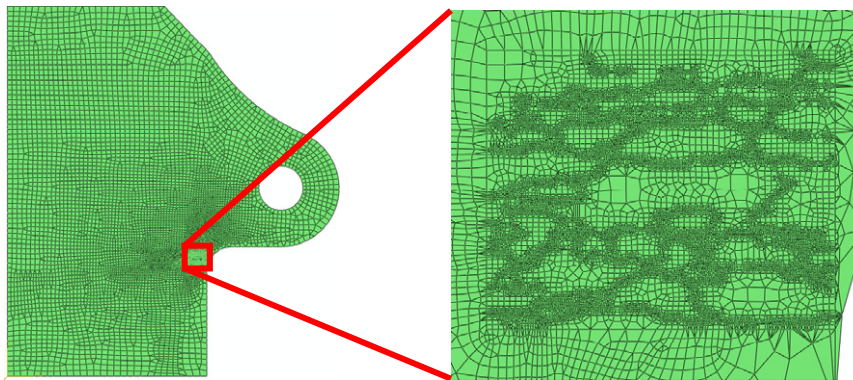


Fig. 6. Finite element mesh of lug joint.

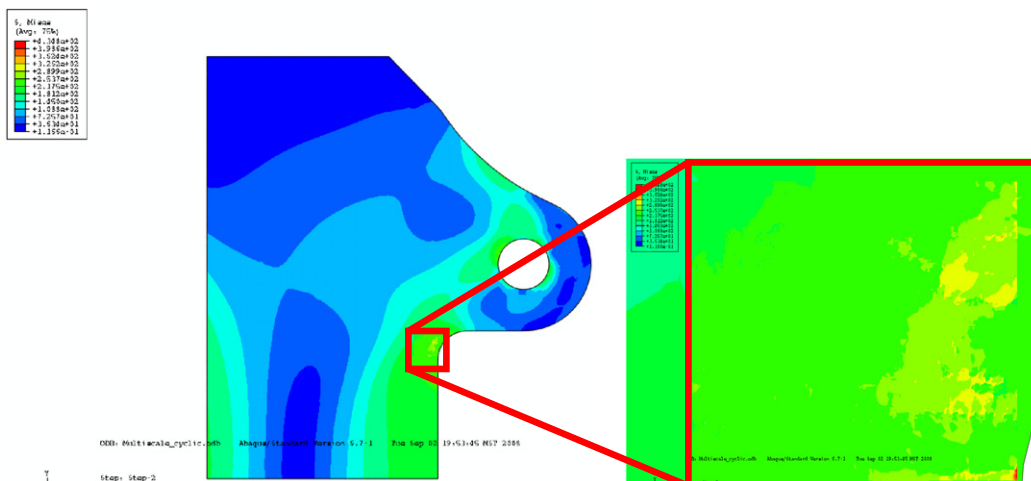


Fig. 7. Mises stress distribution of lug joint.

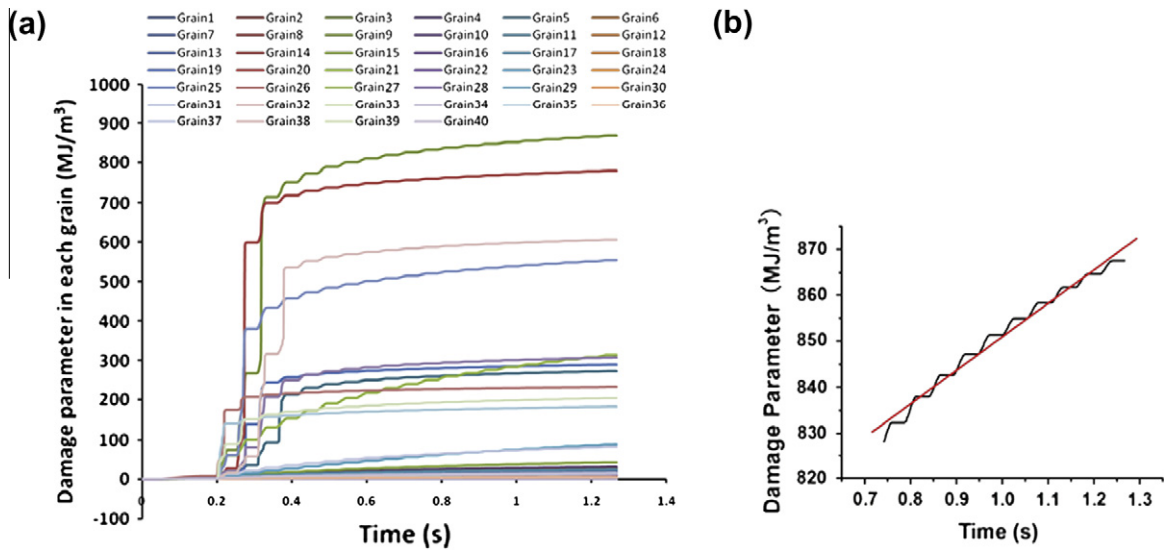


Fig. 8. (a) Damage evolution in each grain for 20 cycles, and (b) an example shows that damage grows linearly after 10 cycles in each individual grain.

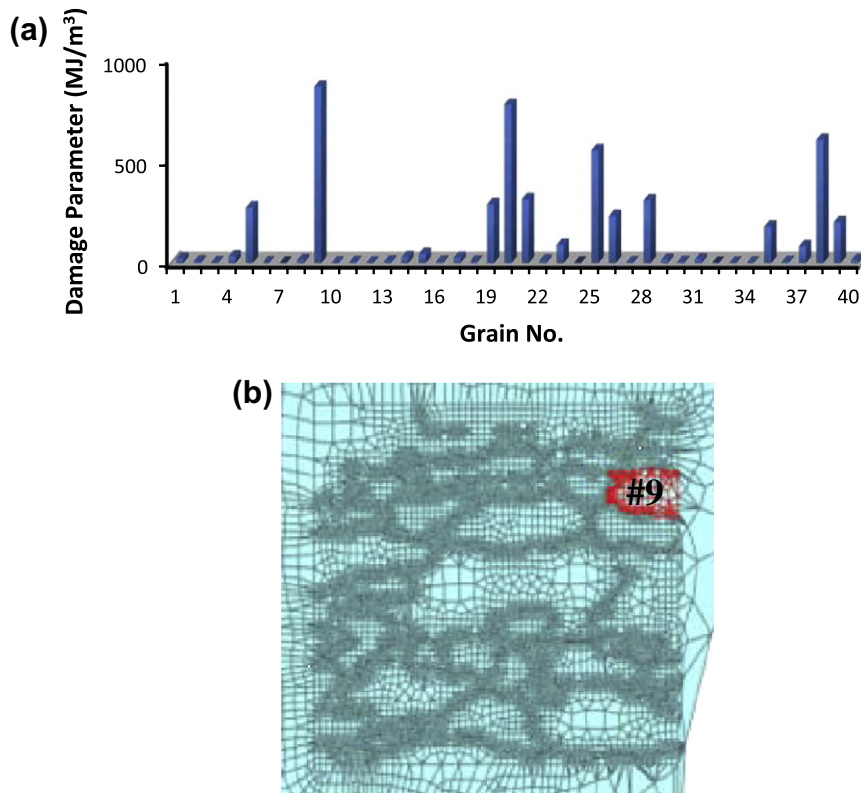


Fig. 9. (a) Damage distribution in RVE for all grains, and (b) location of critical grain.

density ω . The equation to determine a critical damage value is presented below:

$$D_c = \frac{2 \times \omega \times l}{A} \quad (19)$$

4. Results and validation

4.1. Lug joint fatigue tests

The lug joint is one of the several ‘hotspots’ in aerospace structures that experience fatigue damage. The fatigue tests were per-

formed on lug joint samples prepared from an Al 2024 T351 plate. An Instron 1331 hydraulic load frame was used to apply load to the samples. Fig. 5 shows the experimental setup of the test. A digital image acquisition system was used to collect pictures from a CCD camera to monitor potential locations of crack initiation and measuring crack length. A cyclic loading of 490 N (110 lbs) to 4900 N (1100 lbs) with a frequency of 20 Hz in sinusoidal waveform was applied to the lug joint sample through the bottom clevis. From those images taken from the digital image acquisition system, a crack length vs. number of cycles curve can be plotted. Then the number of cycles to get a 1 mm crack in the sample can be interpolated from this curve. Table 4 shows the number of

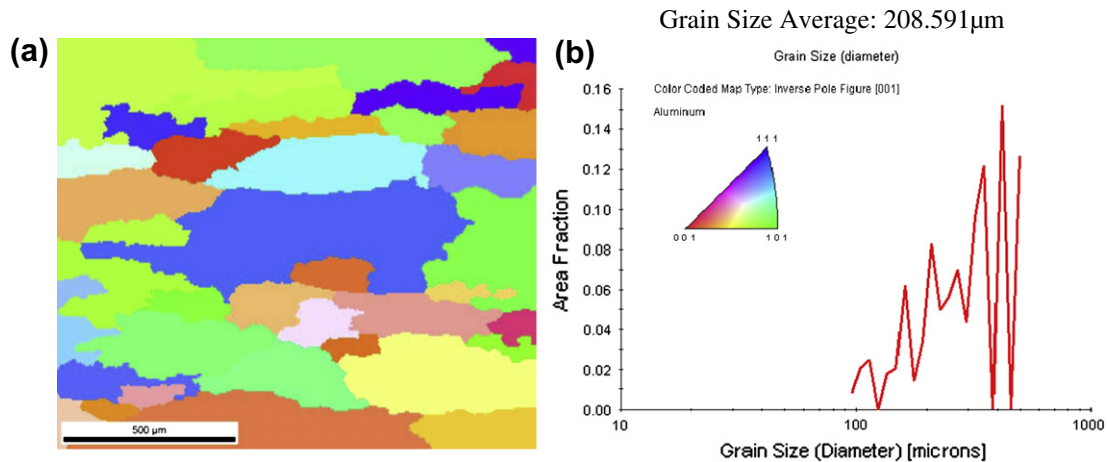


Fig. 10. Microstructure and grain size distribution of the meso RVE.

cycles to obtain a 1 mm crack for different lug specimens. The experiment results for 1 mm crack will be compared with the estimations of the 1 mm × 1 mm meso RVE failure from the simulations. Also the images can be measured to get the initial crack direction on the lug joint specimen and subsequently compared with the potential crack directions obtained from the simulations.

4.2. Numerical simulations

For efficient multiscale analysis of structural components such as a lug joint, a two-scale mesh is needed. The meso RVE mesh generated using the software OOF was used at the hotspot of the lug joint. Detailed procedures are presented in our previous work [29]. The rest of the lug joint is described as a homogenous material. The constitutive relation of this homogeneous material was obtained by homogenizing the meso RVE stress–strain response. First, a force was applied at the right edge of the meso RVE where plane stress elements were used. The UMAT based on single crystal plasticity was used to describe material behavior for each grain within the meso RVE. Then, the displacement of each node at the edge was calculated. The corresponding homogenized meso RVE stress–strain response can be plotted according to the applied load and the displacement of each node. This curve was used to perform the plane stress simulations [29]. The two-scale mesh was generated using the commercial software Altair Hypermesh. Fig. 6 shows the two-scale mesh of the lug joint. CPS3 and CPS4 elements are used for the FE simulations of the lug joint to investigate the surface of the specimen. Symmetric boundary conditions were used for simulation so that only half of the lug joint was analyzed in the ABAQUS. The load condition is the same as the fatigue test from 490 N (110 lbs) to 4900 N (1100 lbs) with a frequency of 20 Hz in sinusoidal waveform at the pin hole of the lug. Fig. 7 shows the von Mises stress distribution in the lug joint under simple tension and the non-uniform distribution within the hotspot due to different grain orientations.

The previously described damage tensor was implemented in the UMAT and a data processing code was also developed in Matlab. Using the finite element analysis results, damage evolution for all grains in the meso RVE is plotted in Fig. 8 for 20 cycles. Fig. 8 shows that after 10 cycles, the damage evolution in each grain becomes stable which provides a basis to use a linear fit to extrapolate the damage evolution in individual grains. It should be noted that, the purpose of this paper is to propose a new methodology for fatigue damage prediction considering microstructure features. All simulations here are under constant cyclic loading. Thus, the

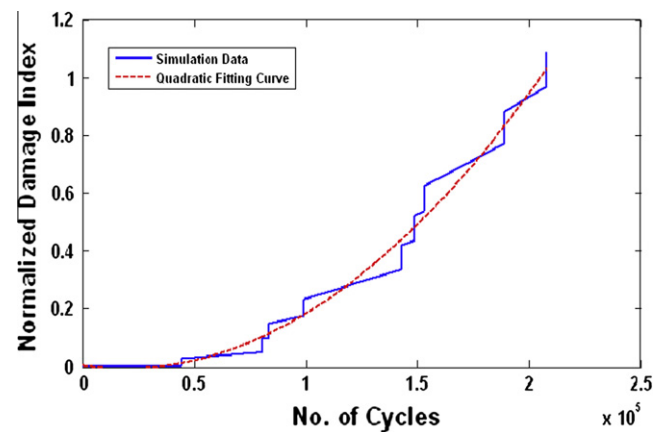


Fig. 11. Normalized damage index for meso RVE vs. no. of cycles.

damage evolution in each grain becomes approximately linearly after 10 cycles. For random load condition, future work will be addressed on building the relationship between the apply load and the damage growth in each individual grain. Fig. 9a shows the damage parameter of all the grains within the RVE at the time $t = 1.2667$ s and Fig. 9b presents the enlarged area of the RVE and highlight the crack initiation area where the damage parameter was maximum. This critical grain is labeled as grain No. 9 shown in Fig. 9a. The results confirm that the critical grain in the RVE is located close to the free surface at the shoulder of the lug joint.

A Matlab program was built in for post-processing of finite element results. Fig. 10 shows the microstructure and the grain size distribution of the meso RVE being used. Fig. 11 shows the normalized damage parameter for the meso RVE vs. the number of cycles. The simulation data fit a quadratic polynomial well, which is intuitive given that as more grains reach the critical damage value, the accumulation of damage in the meso RVE accelerates. The estimated number of cycles until failure in the meso RVE, i.e. when the normalized damage index of the meso RVE reaches 1, is 208 k cycles. Result of simulation matches well with the experimental results of sample 1–3 shown in Table 4. At the same time, the corresponding eigenvector, an indicator of the potential damage direction, is calculated by the weighted average method from all the grains. For this work, all the simulations were carried out in a 2D surface. A histogram showing the appearance frequency of the corresponding eigenvector angle with respect to

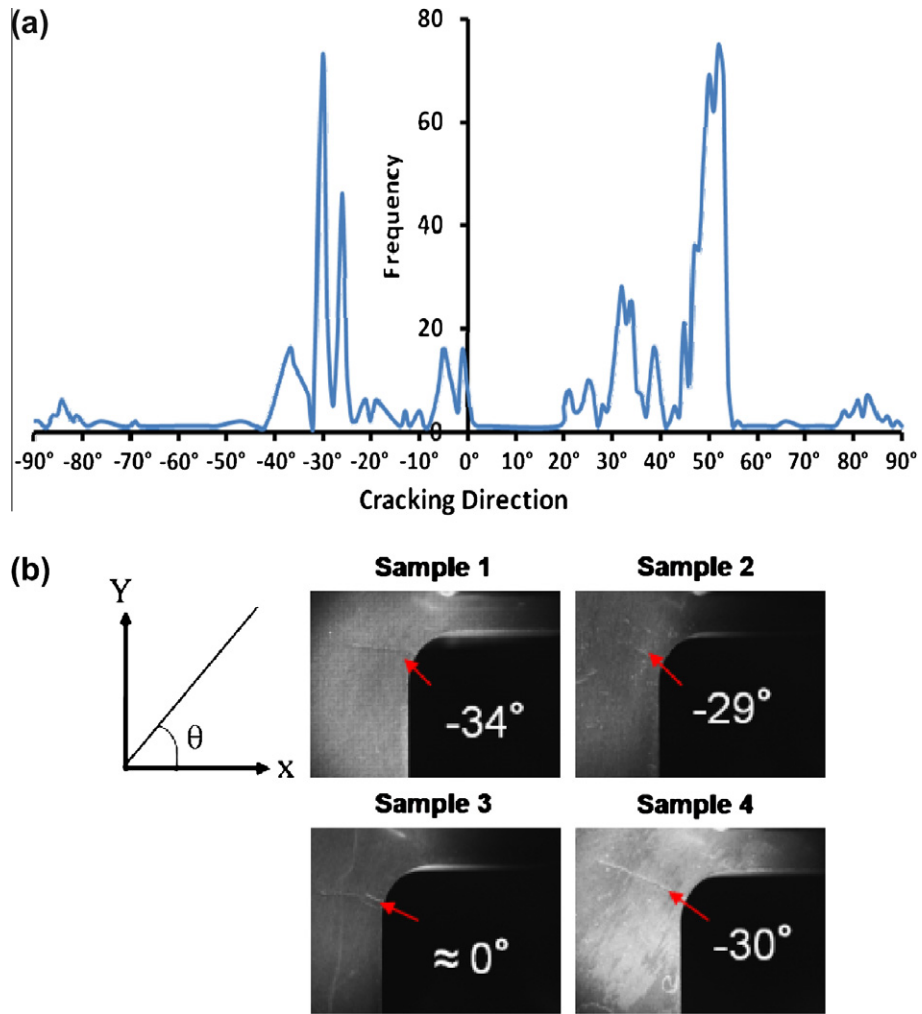


Fig. 12. (a) Histogram of damage direction in RVE, and (b) cracking directions from fatigue tests.

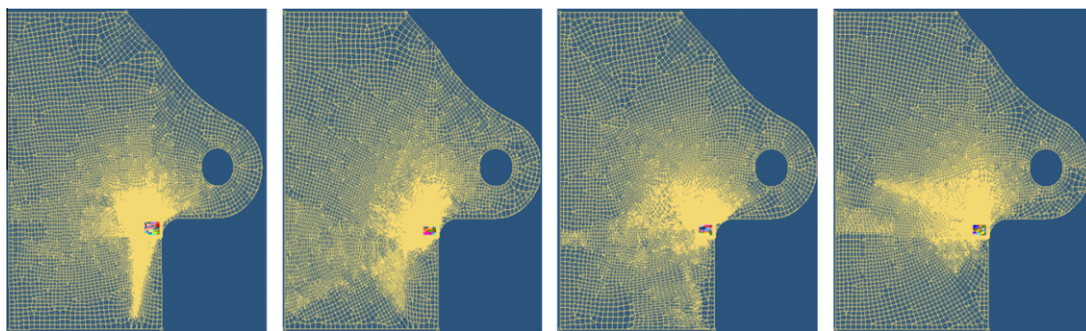


Fig. 13. Finite element meshes of different lug joints.

Table 5

Average grain size and estimation of failure for different meso RVEs.

Lug joint simulations	Simulation 1	Simulation 2	Simulation 3	Simulation 4	Simulation 5
Average grain size (μm)	208.591	191.866	190.266	242.684	191.082
Estimate failure of RVE (k cycles)	208	184	298	177	116

the horizontal direction is shown in Fig. 12a to determine the most potential damage for the meso RVE. The figure indicates that the directions of maximum damage in the RVE, obtained from

simulation, are approximately -30° and 52° . The experimental crack directions from lug joint fatigue tests are shown in Fig. 12b.

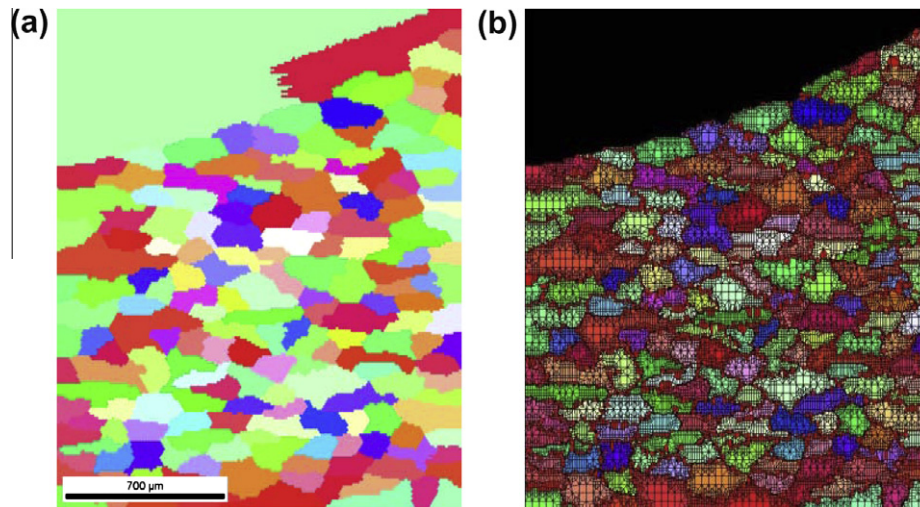


Fig. 14. (a) EBSD scan directly from the shoulder of lug joint sample, and (b) finite element meshes created from OOF.

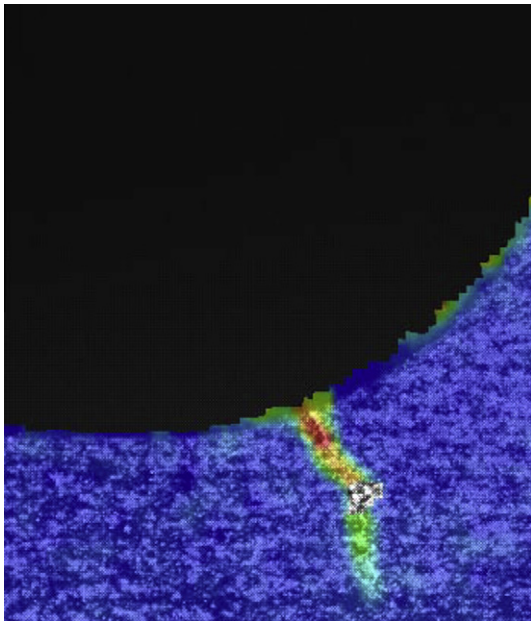


Fig. 15. Crack reaches 1.5 mm.

Further simulations were conducted to verify the developed model and consider uncertainty of the meso RVE shown in Fig. 13. The same lug joint with only one meso RVE located at the shoulder was used. However, the meso RVEs contain different oriented grains and different number of grains. As mentioned before, all meso RVEs' sizes are approximated to $1 \text{ mm} \times 1 \text{ mm}$. The average grain size and the estimated failure of meso RVEs are shown in Table 5.

It should be noted that the estimation of RVE failure in simulation 5 is close to the fatigue test in sample 4. Variability in the simulation results indicates that the fewer number of cycles required in sample 4 to obtain a 1 mm crack could be because of different oriented grains. Further validations will be performed to investigate these results.

The five simulations suggested that grain orientation will affect the estimation of RVE failure. The common feature for all five simulations is that, the RVEs are taken from the same Al alloy plate from which the lug joint samples were made. However, RVEs obtained from the scans are not directly from the lug joint samples which results in the variability of the input data for the model. To prevent the variability of the input data, a RVE directly scanned from the lug joint shoulder was created (shown in Fig. 14). The procedure is to obtain four scans from both shoulders of the lug joint on both sides and to conduct fatigue test on the same lug joint sample to determine which scan should be used in the simulation for validation. For this fatigue test, the loading was changed from

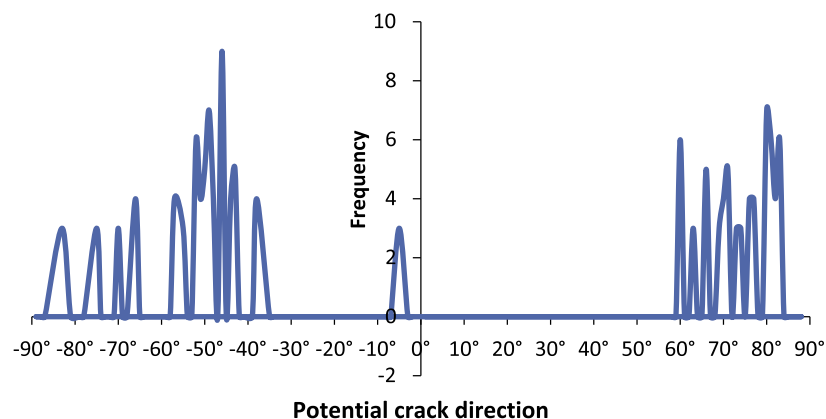


Fig. 16. Histogram for potential crack direction.

150 lbs to 1500 lbs. Because of the high loading condition and high frequency, the number of cycles to obtain a 1 mm crack in the lug joint was not recorded. The lowest number of cycles recorded was 33 k cycles for a 1.5 mm crack (shown in Fig. 15).

The simulation result of RVE failure is found to be 12.4 k cycles. Considering the number of cycles required for short crack propagation up to 1.5 mm obtained experimentally, the authors believe the simulation result is acceptable. The direction of crack propagation at the early stage of fatigue test is around -53° with respect to the horizontal direction as shown in Fig. 15. The histogram of the simulation for potential crack direction is presented in Fig. 16. Results show two major potential crack direction bands. One is from around -58° to -43° and the other one is from 60° to 85° . The experiment result showed that the crack propagated along one of the potential crack direction range obtained from the simulation, indicating that the model can predict potential crack directions.

5. Conclusion

A multiscale damage criterion that captures damage initiation at the microscale has been developed. This criterion focuses on the crack initiation in fatigue life. Experimental observation of fatigue test on lug joint shows that the fatigue life is significant prior to crack initiation that can be detectable by available sensors and SHM techniques. Once the initiation happens, crack growth rate is very high. This makes damage initiation very important for estimating structural fatigue life. This paper shows the authors' current effort on estimation of fatigue life up to the physically small crack (1 mm). The results show that the estimation of RVE failure at a structural hotspot under cyclic loading obtained from the multiscale damage criterion match the number of cycles needed to get a 1 mm crack in the structural component from the experiment. In addition, the damage criterion has the capability to provide the potential directions for crack growth. Future work will focus on extension of the damage criterion for short and long crack propagation and the application of the damage information obtained to structural health monitoring and prognosis.

Acknowledgments

This research is supported by the Department of Defense, AFOSR Multidisciplinary University Research Initiation (MURI) Grant, FA95550-06-1-0309, Technical Monitor Dr. David S. Stargel.

Thanks to Dr. Peralta and his group from Arizona State University for the experimental support in this research work.

References

- [1] Chang P, Liu S. Recent research in nondestructive evolution of civil infrastructures. *J Mater Civil Eng* 2003;298:304.
- [2] Frangopol D, Peil U. Life-cycle assessment and life extension of structures via innovative methods. In: *Proceedings of the third European workshop on structural health monitoring*; 2006. p. 49–57.
- [3] Farrar C, Worden K. An introduction to structural health monitoring. *Philos Trans Roy Soc* 2007;1:303–15.
- [4] US Air Force Scientific Advisory Board. Report of the AdHoc committee on air force aircraft jet engine manufacturing and SAF/AQQS. Washington, DC: The Pentagon; 1992.
- [5] Lemaitre J, Desmorat R. *Engineering damage mechanics*. New York, Berlin, Heidelberg: Springer; 2005.
- [6] Stephens RI, Fatemi A, Fuchs RR, Stephens HO. *Metal fatigue in engineering*. 2nd ed. Wiley; 2000.
- [7] Frost NE, Marsh KJ, Pook LP. *Metal fatigue*. Oxford: Clarendon Press; 1974.
- [8] Kocanda S. *Fatigue failures of metals*. Netherlands: Sijthoff and Noordhoff International Publishers; 1978.
- [9] Klesnil M, Lukas P. *Fatigue of metallic materials*. Elsevier Science & Technology; 1992.
- [10] Forsyth PJE. *The physical basis of metal fatigue*. American Elsevier Pub., Co.; 1969.
- [11] Schijve J. Significance of fatigue cracks in micro-range and macro-range. *ASTM STP* 415; 1967. p. 415–59.
- [12] Shang DG, Yao WX, Wang DJ. A new approach to the determination of fatigue crack initiation size. *Int J Fatigue* 1998;20(9):683–7.
- [13] Miller KJ. The behavior of short fatigue cracks and their initiation. Part I. A review of two recent books. *Fatigue Fract Eng Mater Struct* 1987;10:75–91.
- [14] Miller KJ. The behavior of short fatigue cracks and their initiation. Part II. A general summary. *Fatigue Fract Eng Mater Struct* 1987;10:93–113.
- [15] Ritchie RO, Lankford J. Small fatigue cracks: a statement of the problem and potential solutions. *Mater Sci Eng* 1989(1–2):11–6.
- [16] Taylor G. The mechanism of plastic deformation of crystals. Part I. – theoretical. *Proc Roy Soc Lond* 1934:362–87.
- [17] Taylor G. Plastic strain in metals. *J Inst Metal* 1938:307–25.
- [18] Hill R. Generalized constitutive relations for incremental deformation of metal crystals by multislip. *J Mech Phys Solids* 1966;9:5–102.
- [19] Rice J. Inelastic constitutive relations for solids: an internal-variable theory and its application to metal plasticity. *J Mech Phys Solids* 1971:33–455.
- [20] Hill R, Rice JR. Constitutive analysis of elastic–plastic crystals at arbitrary strain. *J Mech Phys Solids* 1972:401–13.
- [21] Asaro R, Rice J. Strain localization in ductile single crystals. *J Mech Phys Solids* 1977:309–38.
- [22] Asaro R. Crystal plasticity. *J Appl Mech* 1983:921–34.
- [23] Asaro R. Micromechanics of crystals and polycrystals. *Adv Appl Mech* 1983:1–115.
- [24] Bassani J. Plastic flow of crystals. *Adv Appl Mech* 1994:191–258.
- [25] Horstemeyer MF, McDowell DL, McGinty RD. Design of experiments for constitutive model selection: application to polycrystal elastoplasticity. *Model Simul Mats Sci Eng* 1999;7:253–73.
- [26] Horstemeyer MF, McDowell DL. Modeling effects of dislocation substructure in polycrystal elastoplasticity. *Mech Mater* 1998;27:145–63.
- [27] ABAQUS, Abaqus/CAE and abaqus/standard, Ver. 6.7. Simulia world headquarters, providence; 2007.
- [28] Huang Y. A user-material subroutine incorporating single crystal plasticity in the ABAQUS finite element program. Harvard University: Mech report 178. Division of Engineering and Applied Sciences; 1991.
- [29] Luo C, Wei J, Parra-Garcia M, Chattopadhyay A, Peralta P. Fatigue damage prediction in metallic materials based on multiscale modeling. *AIAA J* 2009;47:2567–76.
- [30] Parra-Garcia M, Luo C, Noshadravan A, Keck A, Teale R, Chattopadhyay A, et al. Microstructure representation and material characterization for multiscale finite element simulations of local mechanical behavior in damaged metallic structures. In: *Proceedings of SPIE smart structures and materials & nondestructive evaluation and health monitoring, invited session on information management for structural health monitoring*, San Diego, California, March 2008.
- [31] Jiang Y. A fatigue criterion for general multiaxial loading. *Fatigue Fract Eng Mater Struct* 2000;23(1):19–32.
- [32] Ding F, Zhao T, Jiang Y. A study of fatigue crack growth with changing loading direction. *Eng Fract Mech* 2007(13):2014–29.
- [33] Kalnaus S, Jiang Y. Fatigue life prediction of copper single crystals using a critical plane approach. *Eng Fract Mech* 2006(6):684–96.
- [34] Laird C. The influence of metallurgical structure on the mechanisms of fatigue crack propagation. *Fatigue crack propagation*, ASTM STP 415, Philadelphia; 1967. p. 131–80.
- [35] Neumann P. New experiments concerning the slip processes at propagating fatigue cracks-I. *Acta Metall* 1974;22:1155–65.
- [36] Haftka RT, Gürdal Z. *Elements of structural optimization*. Netherlands: Kluwer Academic Publishers; 1992.
- [37] Garruchet S, Politano O, Salazar JM, Montesin T. An empirical method to determine the free surface energy of solids at different deformations and temperature regimes: an application to Al. *Surf Sci* 2005;586(1–3):15–24.